Cosmoglobe DR2. IV. Modelling starlight in DIRBE with *Gaia* and WISE

M. Galloway[1]⋆, E. Gjerløw[1], M. San[1], R. M. Sullivan[1], D. J. Watts[1], R. Aurvik[1], A. Basyrov[1], L. A. Bianchi[1], A. Bonato[2], M. Brilenkov[1], H. K. Eriksen[1], U. Fuskeland[1], K. A. Glasscock[1], L. T. Hergt[3], D. Herman[1], J. G. S. Lunde[1], A. I. Silva Martins[1], D. Sponseller[4], N.-O. Stutzer[1], H. Thommesen[1], V. Vikenes[1], I. K. Wehus[1], and L. Zapelli[2,5,6]

[1] Institute of Theoretical Astrophysics, University of Oslo, Blindern, Oslo, Norway
[2] Dipartimento di Fisica, Università degli Studi di Milano, Via Celoria, 16, Milano, Italy
[3] Laboratoire de Physique des 2 infinis – Irène Joliot Curie (IJCLab), Orsay, France
[4] Department of Space, Earth and Environment, Chalmers University of Technology, Gothenburg, Sweden
[5] Università di Trento, Università degli Studi di Milano, CUP E66E23000110001
[6] INFN sezione di Milano, 20133 Milano, Italy

January 13, 2026

ABSTRACT

We present a model of starlight emission in the Diffuse Infrared Background Explorer (DIRBE) data between 1.25 and 25 μm based on *Gaia* and WISE measurements. We include two classes of compact objects, namely bright stars with individual spectral energy densities (SEDs) measured by *Gaia*, and a combined diffuse background of dim point source emission. Of the 424 829 bright sources that we fit, the number of stars with a flux density detected by WISE at Galactic latitudes $|b| > 20°$ at more than 5σ is 94 680, for an average of 1.36 stars per DIRBE beam area. For each star, we adopt physical parameters ($T_{\rm eff}$, log g, and [M/H]) from *Gaia*; use these to identify a best-fit effective SED with the PHOENIX stellar model library; convolve with the respective DIRBE bandpass; and fit an overall free amplitude per star within the Bayesian end-to-end Cosmoglobe DR2 framework. The contributions from faint sources are accounted for by coadding all 710 825 587 WISE sources not included as bright stars, and fit one single overall amplitude per DIRBE band. Based on this model we find that total star emission accounts for 91 % of the observed flux density at 2.2 μm; 54 % at 4.9 μm; and 1 % at 25 μm. As shown in companion papers, this new model is sufficiently accurate to support high-precision measurements of both the Cosmic Infrared Background monopole and zodiacal light emission in the three highest DIRBE frequencies.

Key words. ISM: general - Zodiacal dust, Interplanetary medium - Cosmology: observations, diffuse radiation - Galaxy: general

1. Introduction

Modelling the astrophysical sky using the *COBE*-Diffuse Infrared Background Explorer (DIRBE; Hauser et al. 1998) data from 1 to 100 000 GHz requires an understanding of all the various components that make it up. At the highest of these frequencies, the largest power contribution comes from resolved stars in our galaxy, as well as an unresolved background of dimmer sources. The four shortest wavelength/highest frequency DIRBE bands between 1.25 and 4.9 μm are all dominated by star emission (Arendt et al. 1998), making accurate star modelling essential for using these data in combination with others in a comprehensive Bayesian model of the large-scale infrared sky (Watts et al. 2024a). Additionally, point sources are also subdominant contributors in the DIRBE 12 and 25μm channels, which if not handled correctly could bias derived constraints on the zodiacal light and other components (Kelsall et al. 1998; San et al. 2024).

Many full-sky datasets exist which measure the emissions from point sources in our galaxy and beyond. Starting with *IRAS* in 1983 (Neugebauer et al. 1984), there have been several ground and space missions to map the infrared sky and put constraints on star formation and evolution, the Cosmic Infrared Background (CIB) and Active Galactic Nuclei (AGN), including the Infrared Space Observatory (ISO; Kessler et al. 1996), Spitzer (Werner et al. 2004), the 2-Micron All-Sky Survey (2MASS) (Skrutskie et al. 2006), and the current-generation James Webb Space Telescope (JWST) (Gardner et al. 2006). For the purposes of compatibility with the DIRBE data, however, the most useful external datasets are the Wide-Field Infrared Survey Explorer (WISE) (Wright et al. 2010), and *Gaia*, which produced high precision star observations at optical wavelengths (Gaia Collaboration et al. 2023; Brown et al. 2018).

In this paper, which is part of the larger Cosmoglobe DR2 results paper suite (Watts et al. 2024a, and references therein), we discuss the modelling of compact objects in DIRBE as part of our larger full sky astrophysical model. Section 2 discusses this modelling in a larger Bayesian context. Section 3 shows the astrophysical results of the works by presenting a unified star model and its associated errors. Section 4 then shows the consistency between our results and other work in this area. Finally, we conclude in Sect. 5, discussing the impacts of this work and offering some avenues for future research.

2. Bayesian star modelling in Cosmoglobe DR2

In this work, we define two categories of stars, which are treated differently but jointly. The first category includes objects in the AllWISE 3.4 μm catalog (Wright et al. 2009) with a magnitude brighter than 7, but excluding sources that are spatially too close to distinguish with the DIRBE beam. This comprises a total of

---

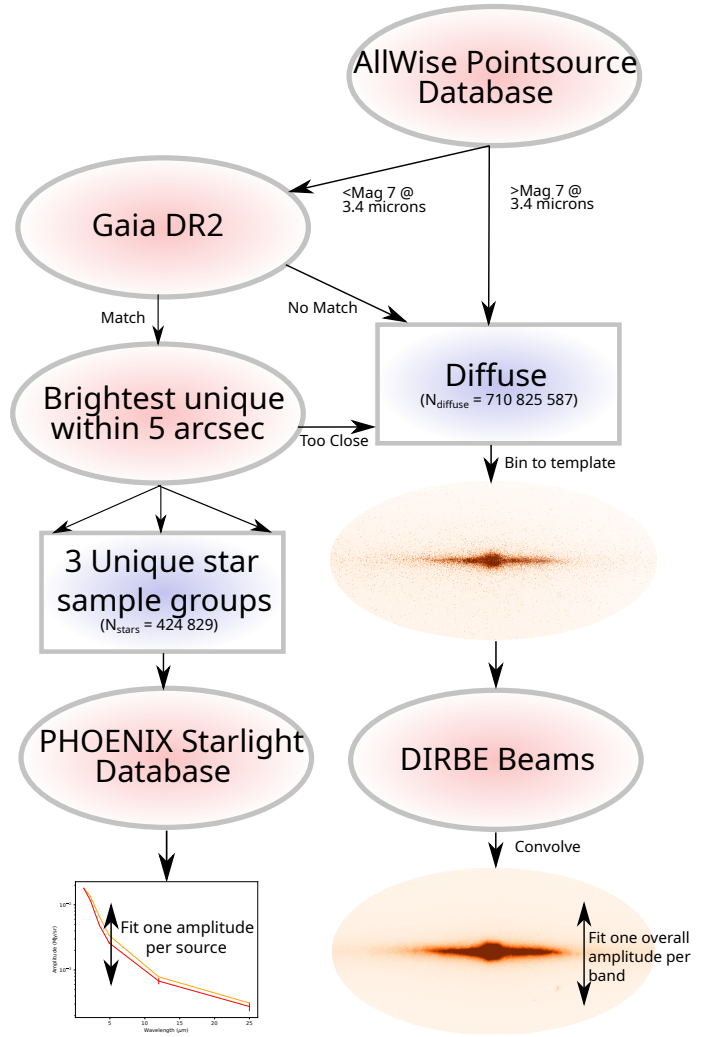⋆ Corresponding author: M. Galloway; mathew.galloway@astro.uio.no
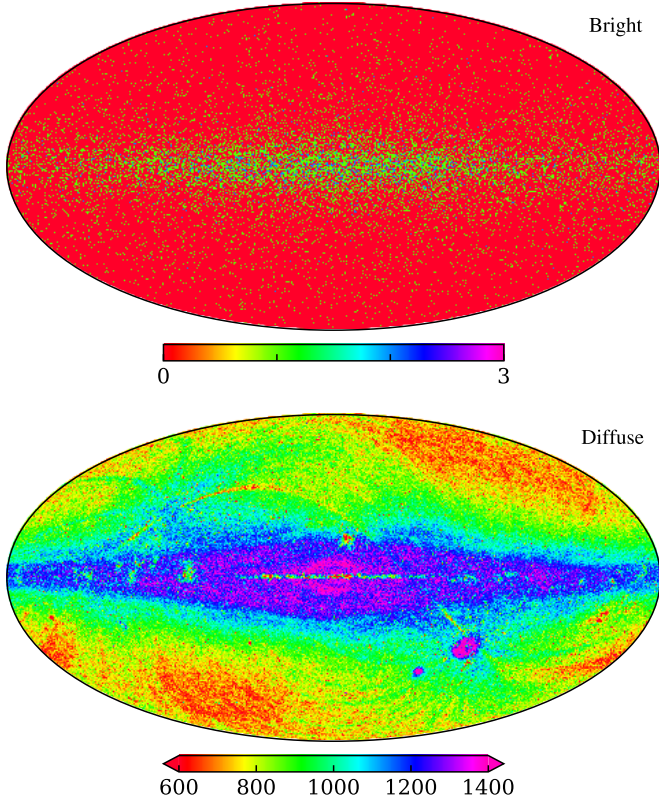
Fig. 1. Top: Total number of bright sources in each pixel. Bottom: Total number of sources included in the diffuse template, which shows a clear imprint of the WISE scan strategy.

Fig. 2. Schematic diagram of the CosmoGlobe DR2 compact object processing pipeline. Red ovals represent input data, and the blue boxes indicate the two classes of sources described in this paper.
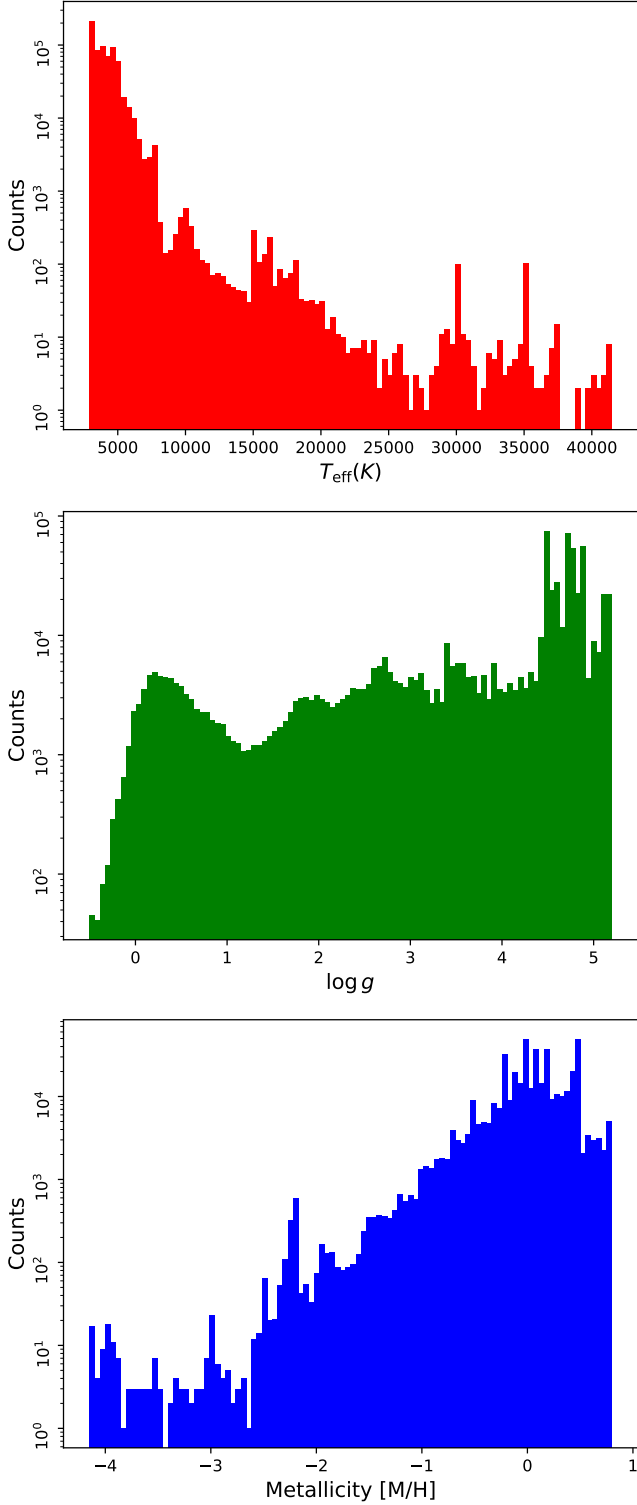
424 829 bright objects, and the top panel of Fig. 1 shows the distribution of these across the sky in terms of the total number of stars per HEALPix[1] map (Górski et al. 2005) 7′ pixel (N_{side} = 512). Each of these stars are modelled individually using data from *Gaia* in the current analysis, as described in Sect. 2.2. The second category includes all the other sources in the AllWISE catalog, which comprises a total of 710 825 587 objects. The distribution of these are shown in the bottom panel of Fig. 1. In the current analysis, these are all co-added into one effective spatial template of the dimmer "background", and we will hereafter refer to this as the "diffuse" component; for details, see Sect. 2.3. An overview of the full compact object processing pipeline used in this analysis is shown in Fig. 2.

2.1. Data model and sampling algorithm

The objective of this paper is to fit the amplitude of both individual bright stars and the overall diffuse background jointly as part of the global Bayesian CosmoGlobe DR2 analysis framework. The details of this process are discussed by Watts et al. (2024a); San et al. (2024); Gjerløw et al. (2026b), and here we only give a brief review of the main points that are directly relevant for starlight modelling.

The basic CosmoGlobe DR2 data model takes the following form,

$$d = \text{GPB} \sum_{c=1}^{n_{\text{comp}}} \text{M}_c \boldsymbol{a}_c + \boldsymbol{s}_{\text{zodi}} + \boldsymbol{s}_{\text{static}} + \boldsymbol{n}_{\text{corr}} + \boldsymbol{n}_{\text{w}} \quad (1)$$

$$\equiv \boldsymbol{s}_{\text{tot}} + \boldsymbol{n}_{\text{w}}, \quad (2)$$

where $\boldsymbol{d}$ indicates time-ordered data; G represents instrumental gain; P encodes the telescope pointing; B denotes beam convolution; M_c is a so-called mixing matrix that defines the relative strength of component c at frequency ν; $\boldsymbol{a}_c$ is a reference component amplitude; $\boldsymbol{s}_{\text{zodi}}$ and $\boldsymbol{s}_{\text{static}}$ are contributions from zodiacal light; and $\boldsymbol{n}_{\text{corr}}$ and $\boldsymbol{n}_{\text{w}}$ are correlated and white instrumental noise, respectively. We note that not all parameters are fitted for all channels; see Watts et al. (2024a) for details.

As far as this paper is concerned, the key element is $\text{M}_c \boldsymbol{a}_c$, which defines the astrophysical sky model. In general, this expression includes terms for each relevant physical process, which for the current analysis are thermal dust (Gjerløw et al. 2026a; Sullivan et al. 2026; Gjerløw et al. 2026b), free-free (Dickinson et al. 2003; Planck Collaboration X 2016), CIB (monopoles; Hauser et al. 1998; Watts et al. 2024b), and the two starlight populations introduced above. Explicitly, we adopt the follow-

---

[1] http://healpix.sourceforge.net

where U_{mJy} is a unit conversion factor; $\epsilon_j(\nu)$ is a frequency-dependent extinction factor; f_{Gaia} is a (bandpass-convolved) Spectral Energy Density (SED) amplitude per channel and source; and $\boldsymbol{a}_{\mathrm{s},j}$ is the amplitude per source, which is the only parameter that is fitted freely per object. Finally, the second term simply consists of a single overall diffuse template, $\boldsymbol{t}_{\mathrm{diff}}$, multiplied with a free template amplitude per channel. The definition and construction of each of these factors are described in Sects. 2.2 and 2.3.

As noted above, the CosmoGlobe DR2 algorithm is a Gibbs sampler, which in practice means that we sample one parameter in Eq. 1 at a time, while keeping all others temporarily fixed, and then iterate through all parameters. As far as the current paper is concerned, the key steps are therefore to be able to sample from the two following conditional distributions,

$$\boldsymbol{a}_{\mathrm{bright}} \leftarrow P(\boldsymbol{a}_{\mathrm{bright}}|\boldsymbol{d}, \mathsf{G}, \mathsf{M}_{\mathrm{dust}}, \boldsymbol{a}_{\mathrm{dust}}, \boldsymbol{s}_{\mathrm{zodi}}, \boldsymbol{s}_{\mathrm{static}}, \boldsymbol{n}_{\mathrm{corr}}, a_{\mathrm{diff}}), \quad (5)$$

$$\boldsymbol{a}_{\mathrm{diff}} \leftarrow P(\boldsymbol{a}_{\mathrm{diff}}|\boldsymbol{d}, \mathsf{G}, \mathsf{M}_{\mathrm{dust}}, \boldsymbol{a}_{\mathrm{dust}}, \boldsymbol{s}_{\mathrm{zodi}}, \boldsymbol{s}_{\mathrm{static}}, \boldsymbol{n}_{\mathrm{corr}}, a_{\mathrm{bright}}). \quad (6)$$

As described by Watts et al. (2024a), in practice this is achieved by 1) subtracting the time-domain correction terms ($\boldsymbol{s}_{\mathrm{zodi}}$, $\boldsymbol{s}_{\mathrm{static}}$, and $\boldsymbol{n}_{\mathrm{corr}}$) from the raw time-ordered data; 2) binning the resulting cleaned data into pixelized maps; 3) subtracting all other astrophysical components except the starlight; and 4) drawing $\boldsymbol{a}_{\mathrm{bright}}$ and $\boldsymbol{a}_{\mathrm{diff}}$ from their conditional distribution.

To identify the appropriate conditional distribution, we note that a reduced effective data model may at this point be written in terms of the following signal-plus-noise residual,

$$r = \mathsf{M}_{\mathrm{stars}}\boldsymbol{a}_{\mathrm{stars}} + \boldsymbol{n}_{\mathrm{w}}. \quad (7)$$

Since $\boldsymbol{n}_{\mathrm{w}}$ denotes white Gaussian noise, and M is a fixed matrix, this is a perfectly linear data model in $\boldsymbol{a}$, and the appropriate conditional probability distributions, $P(\boldsymbol{a}_{\mathrm{bright}}|\boldsymbol{d}, \ldots)$ and $P(\boldsymbol{a}_{\mathrm{diff}}|\boldsymbol{d}, \ldots)$, are both Gaussian. The appropriate sampling equation is therefore (see, e.g., Appendix 1 in BeyondPlanck Collaboration 2023)

$$\boldsymbol{a}_i = (\mathsf{M}_i^T \mathsf{N}^{-1} \mathsf{M}_i)^{-1} \mathsf{M}_i \mathsf{N}^{-1} (r - \mathsf{M}_j \boldsymbol{a}_j), \quad (8)$$

where $\{i, j\}$ now denote respectively bright or diffuse sources in a given Gibbs step, and then the reverse combination in the next Gibbs step. This algorithm is then iterated until convergence, and interspersed with similar Gibbs steps for all other free parameters in Eq. 1.

2.2. Bright stars

To complete the above algorithm, we need to specify M, $\boldsymbol{t}$, and $\boldsymbol{n}_{\mathrm{s}}$, and we start by defining the catalog of bright stars. The first step in this procedure is to threshold the AllWise point source catalog (Wright et al. 2009) at magnitude 7 in the W1 band. Many of these are located spatially very close to each other, and given the wide DIRBE beam this results in strong degeneracies in the fitted parameters of nearby objects. Furthermore, as described above, the computational engine of the current analysis framework is a Gibbs sampler, which is known to have a long correlation length for strongly correlated parameters (Geman & Geman 1984). For this reason, we divide the set of bright objects into three separate sampling groups, within each of which no two objects are closer than a given distance. Specifically, each set is constructed by including the brightest remaining object, but only if it is further away from any already included source than 5'. All amplitudes within each group are sampled jointly with sparse matrix operators for the coupling matrix, $(\mathsf{M}_i^T \mathsf{N}^{-1} \mathsf{M}_i)^{-1}$,

Fig. 3. Histograms of the three star parameters taken from *Gaia* (from top to bottom: effective temperature, gravitational acceleration, and metallicity) that are used by the PHOENIX database to determine the star SEDs, for the 424 829 bright stars used in this analysis.

ing data model for the starlight emission in the following,

$$\mathsf{M}_{\mathrm{stars}}\boldsymbol{a}_{\mathrm{stars}} = \sum_{j=1}^{n_{\mathrm{s}}} \mathsf{M}_{\mathrm{bright}}^i \boldsymbol{a}_{\mathrm{bright}}^i + \boldsymbol{a}_{\mathrm{diff}}\boldsymbol{t}_{\mathrm{diff}} \quad (3)$$

$$= U_{\mathrm{mJy}}^i \sum_{j=1}^{n_{\mathrm{s}}} \epsilon_j(\nu) f_{Gaia,j}\boldsymbol{a}_{\mathrm{s},j} + \boldsymbol{a}_{\mathrm{diff}}\boldsymbol{t}_{\mathrm{diff}}, \quad (4)$$

Param	Step Size	Old		Updated	
		Min	Max	Min	Max
T_{eff} (K)	50-100	2300	12000	3000	11900
$\log g$	0.5	0.0	6.0	3.0	5.0
$[M/H]$	0.5	-4.0	1.0	-2.0	1.0

Table 1. Parameters of spectra provided by the PHONEIX starlight database, both for the original and updated spectra.

in Eq. 8, resulting in a vanishing correlation length internally in each group.

For each star in these sampling groups we extract estimates of the effective temperature, T_{eff}, the gravitational acceleration, $\log g$, and the metallicity, $[M/H]$, from the *Gaia* DR2 database (Gaia Collaboration et al. 2018), and use those to identify a best-fit spectral energy density (SED) from the PHOENIX starlight database (Husser et al. 2013). The distributions of these parameters for the selected stars are shown in Fig. 3. Unfortunately, the PHOENIX catalog lacks information for $T_{\mathrm{eff}} > 12000$ K, and so for these we use the closest match; this accounts for 1.1 % of all bright WISE objects. In principle, this may lead to the SEDs of the hottest stars being biased low, but this effect is at least partially mitigated by the fact that we fit the overall amplitude of each star freely in the following analysis.

The relationship between the physical stellar parameters and the resulting star SEDs is illustrated in Fig. 4. The black curves in each panel shows the SED for a typical star with $T_{\mathrm{eff}} = 6000$ K, $\log g = 3$ and $[M/H] = 0$, while the colored curves show the SEDs resulting by changing one parameter at a time. As expected, the effective temperature has the biggest effect on the overall SED, especially when averaged over wide observing bands like those of DIRBE, while the other two parameters only have a relatively mild impact. This is further illustrated in Fig. 5, which shows the ratio between two spectra with $\log g = 5$ and 3, and with the DIRBE channel center frequencies indicated as vertical dashed lines. Here we see that neglecting $\log g$ would lead to a 1-2 % relative bias between the 1.25 and 3.5 μm channels.

2.2.1. The PHOENIX Database

To build an optimal SED model for each stellar source given the parameters retrieved from *Gaia*, a few post-processing steps are needed for the spectra provided by the PHOENIX database. First, PHOENIX provides spectra in finite resolution bins, as summarized in Table 1, whereas the parameters estimated from the *Gaia* data have arbitrary precision. Instead of simply selecting the closest spectrum to each star, we compute a linear combination of the nearest six spectra, weighted by distance from the measured value, as given by

$$s = \frac{1}{3}\left[\frac{s_{T-}(T_+ - T) + s_{T+}(T - T_-)}{T_+ - T_-} \right.$$
$$+ \frac{s_{g-}(g_+ - g) + s_{g+}(g - g_-)}{g_+ - g_-}$$
$$\left. + \frac{s_{M-}(M_+ - M) + s_{M+}(M - M_-)}{M_+ - M_-} \right]. \quad (9)$$

Here, s represents a single spectrum, and we have used T, g and M as short forms for T_{eff}, $\log g$ and $[M/H]$. The subscripts $+$ and $-$ correspond to the closest reference value above and below the measured value (for example, 0.0 and 0.5 if $\log g = 0.315$).
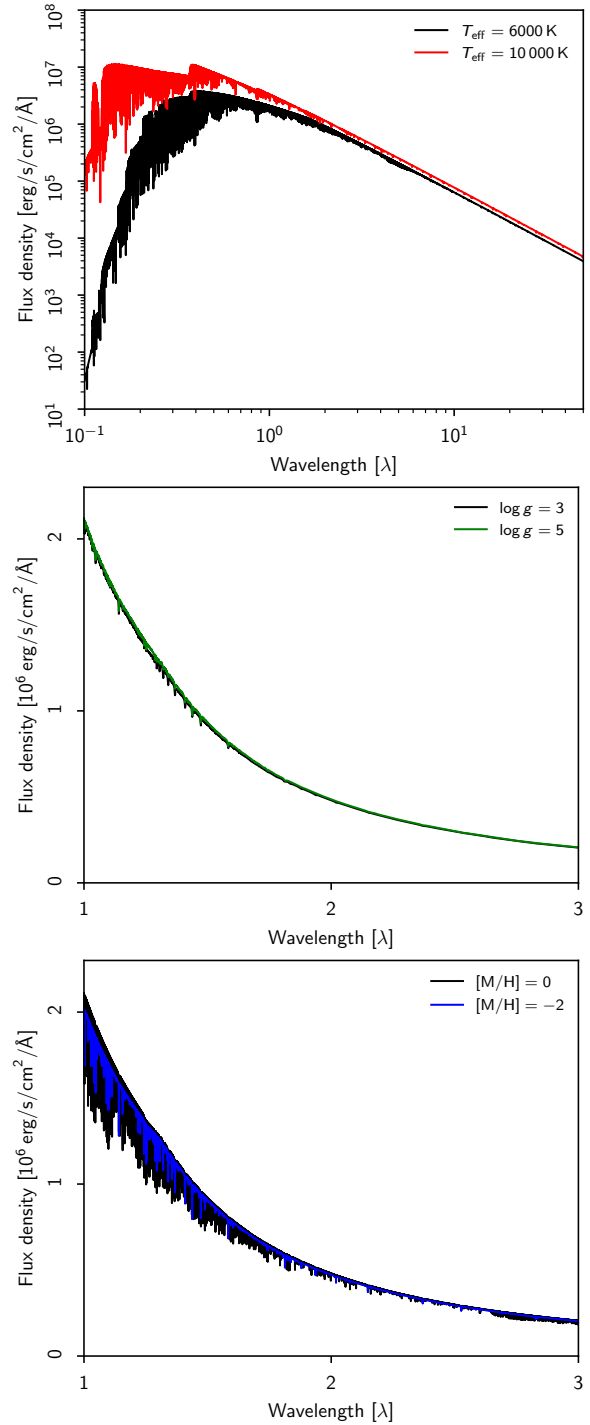
Fig. 4. Comparison of PHOENIX spectra for different parameter combinations. In each panel the black curve shows a reference star spectrum with $T_{\mathrm{eff}} = 6000$K, $\log g = 3.0$ and $[M/H] = 0.0$. The colored curve shows, from top to bottom, the resulting spectra when setting $T_{\mathrm{eff}} = 10\,000$ K, $\log g = 5.0$, and $[M/H] = -2.0$. The spectra shown in the middle panel have been smoothed to highlight the broad features that are mostly relevant for the current analysis.

A second complicating factor is that the updated release of the catalogue[2] contains only a subset of the files in the original catalogue, although they are believed to be more accurate. For stars in the extended parameter range, most importantly those

---

[2] `https://www.astro.uni-jena.de/Users/theory/for2285-phoenix/grid.php`
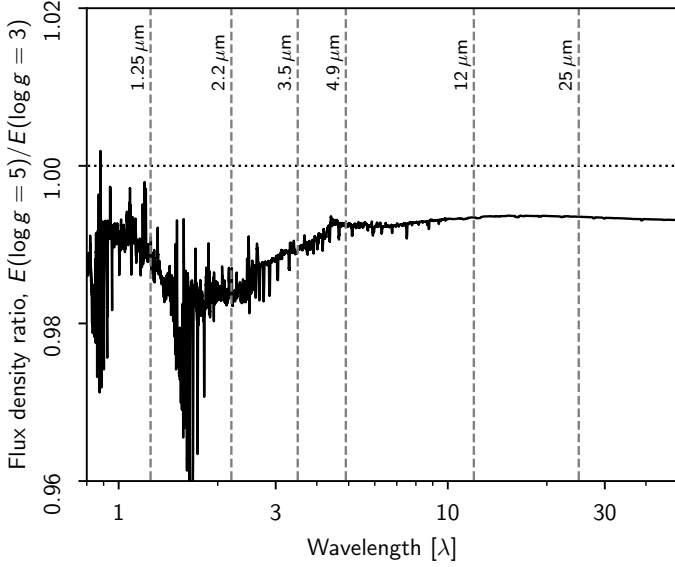
Fig. 5. Ratio between the PHOENIX spectra shown in the middle panel of Fig. 4, corresponding to $E(\log g = 5)/E(\log g = 3)$. The vertical dashed lines indicate the positions of the six shortest wavelength DIRBE channels.
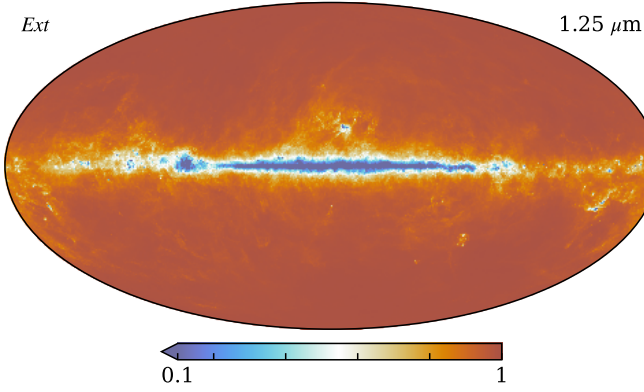
Fig. 6. The full-sky extinction template, ϵ, used in this analysis, evaluated for the DIRBE 1.25μm band.

with $\log g < 3.0$, we therefore calculate spectra using the older files.

Unfortunately, the older files are only defined up to $\lambda = 5.5\,\mu$m, compared to the newer files, which extend to $\lambda = 50\,\mu$m. Amplitude estimates for these stars in the $12\,\mu$m and $25\,\mu$m bands must therefore be determined by first, computing the spectra with the old PHOENIX files and the new PHOENIX files, using the closest endpoint ($\log g = 3.0$ in the most common case). Then, we compute the ratio between the amplitudes of the $3.5\,\mu$m and $4.9\,\mu$m channels, and exploit the observation in Fig. 5 that the spectrum ratio is nearly constant above $4.9\,\mu$m to extrapolate to longer wavelengths.

2.2.2. Binary Stars

About 25% of the stars brighter than magnitude 12 were found to be binary stars in the *Gaia* database, and for many of these, physical parameters are provided for each star separately. When modelling these in DIRBE, which has a low angular resolution, the two contributions must be averaged into one effective SED. For these, we first calculate the spectrum of each component ac-

cording to Eq. 9. Since the flux values are given per unit of area, we then weight the two spectra according to an estimate of the area of the corresponding star, so that the total flux estimated from the binary system reads

$$s_{\mathrm{b}} = \frac{s_1 r_1^2 + s_2 r_2^2}{r_1^2 + r_2^2}, \tag{10}$$

where $s_{1,2}$ and $r_{1,2}$ denote the flux and radius of the respective star in the binary system. The radii are not given explicitly in the *Gaia* catalogue, so we therefore estimate their radius as (Kuiper 1938)

$$r = \exp\left(\frac{3.5 \cdot 4}{5(3.5\log(T_{\mathrm{eff}}) - \log(g))}\right). \tag{11}$$

2.2.3. Extinction

At the highest frequencies, dust extinction becomes important near the Galactic plane. In this paper, we model this effect by $\epsilon(\nu)$, which we define as the ratio between the observed and the intrinsic flux from a given star, i.e., comparing the flux with and without dust extinction. We construct a simplified model for this based on the work by Gordon et al. (2023) and Fitzpatrick et al. (2019). Specifically, we implement their 47-parameter model that extends from UV to infrared frequencies[3], which provides a general sky-averaged estimate of $\epsilon(\nu)$.

To account for spatial variations, we combine this averaged spectral behaviour with the $E(B - V)$ map from the *Planck* 2013 dataset (Planck Collaboration et al. 2014), starting from Eq. 1 of Gordon et al. (2023),

$$\frac{A(\lambda)}{A(V)} = a(\lambda) + b(\lambda)\left[\frac{1}{R(V)} - \frac{1}{3.1}\right]. \tag{12}$$

Here, λ is wavelength, A is the absolute extinction, and a and b are the model coefficients listed by Fitzpatrick et al. (2019). Finally, $R(V)$ is given by

$$R(V) = \frac{A(V)}{E(B - V)}, \tag{13}$$

and therefore denotes the ratio of absolute to selective extinction in the V-band. Substituting this relationship into the above equation, and using the full sky average case of $R(V) = 3.1$ (Fitzpatrick & Massa 1990), allows us to omit the b terms, and we simply obtain

$$A(\lambda) = 3.1\, E(B - V) a(\lambda). \tag{14}$$

Finally, we convert from magnitudes to the linear $\epsilon(\nu)$ scaling factor to obtain

$$\epsilon(\lambda) \equiv \frac{F_{\mathrm{ext}}}{F_{\mathrm{raw}}} = e^{-\frac{3.1}{2.5} E(B-V) a(\lambda)}. \tag{15}$$

The resulting spatial extinction template, evaluated for the 1.25μm band, can be seen in Fig. 6. The majority of the extinction is occurring in the Galactic plane, but additional contributions can be seen tracing dust structures at high galactic latitudes. The template scales according to the relations shown in Fig. 7 of Gordon et al. (2023), and is applied to the stars component as described in Eq. 4.

---

[3] Note that we believe there is a typo in Gordon et al. (2023), which has added an additional negative sign before their value of $b_{IR}\,\alpha_1$. The correct value should be 1.06099.
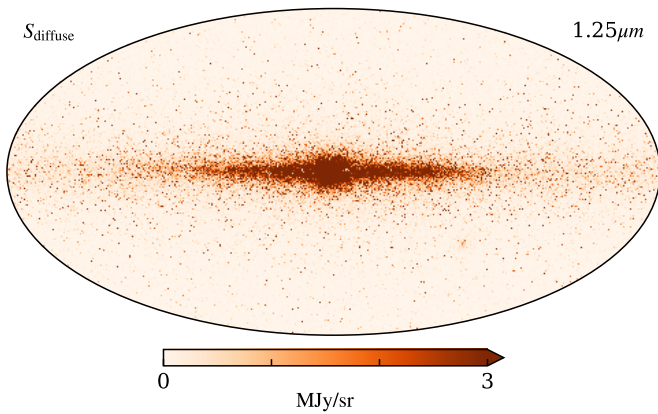
Fig. 7. The unsmoothed template of diffuse star emission evaluated in the DIRBE 1.25μm band. This template is the same for all channels, but with a different overall amplitude.

We conclude this section by noting that this extinction model is indeed simplified, as it does not take into account the actual 3D position of each star, but rather assume the *Planck E(B − V)* map to be valid for any position along a given line of sight. Because most of the high-latitude dust signal observed by *Planck* originates from dust grains closer than a few hundred parsecs from the Sun, while the Galactic plane is filled with dust all through the Milky Way, this approximation is clearly much better at high than low Galactic latitudes. Because of this approximation, we exclude the 1.25 μm channel when estimating a_{bright}, for which extinction is far more important than at longer wavelengths.

2.3. Diffuse Star Emission

After modelling the brightest sources using the method described above, we are left with a diffuse background of stars that are too dim to be individually resolved, but that in aggregate form a significant contribution to the total star signal at these wavelengths and so must be accounted for. We model this diffuse background using a single full-sky template, generated from the WISE W1 data at 3.4 μm. We take the full AllWISE point source catalog, and select all sources with a valid W1 magnitude that are not already included in the bright point source model. To account for pixelization effects, we create this template at high resolution (HEALpix $N_{\mathrm{side}} = 2048$), co-adding over all sources and then downgrade to $N_{\mathrm{side}} = 512$ to match the resolution of the observed DIRBE maps. The resulting map is shown in Fig. 7. This template is then included in the full sky model in Eq. 1, with an amplitude fitted separately for each channel.

3. Astrophysical results

The model described in the previous section is fitted jointly to the DIRBE data together with Galactic dust, zodiacal light, and other components as described by Watts et al. (2024a) and (Gjerløw et al. 2026b). A model of the DIRBE instrument is used to estimate other data artifacts, the most prominent of which was a sun-stationary signal of unknown origins. Following our previous work within the Cosmoglobe framework (BeyondPlanck Collaboration 2023; Watts et al. 2023), we implement this model within the Commander3 codebase (Galloway et al. 2023), which is our Bayesian end-to-end analysis pipeline. The full posterior of all our model parameters was then sampled using Gibbs sampling, exploring the full space around the maximum likelihood
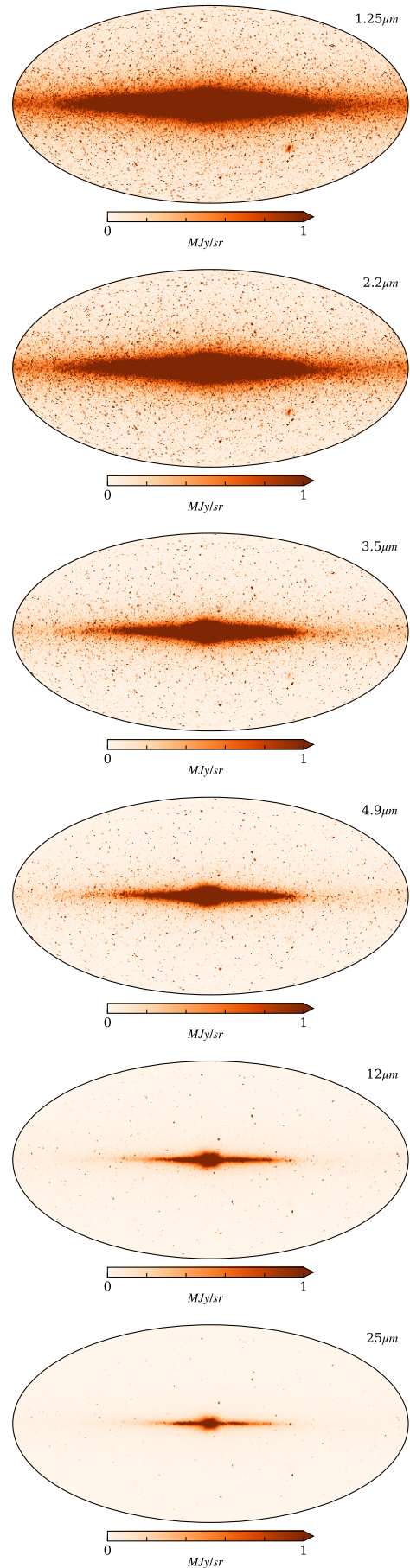
Fig. 8. Posterior mean star maps using the 1090 data samples from the Cosmoglobe DR2 release. These maps are the sum of the bright and diffuse components for the first six DIRBE bands.
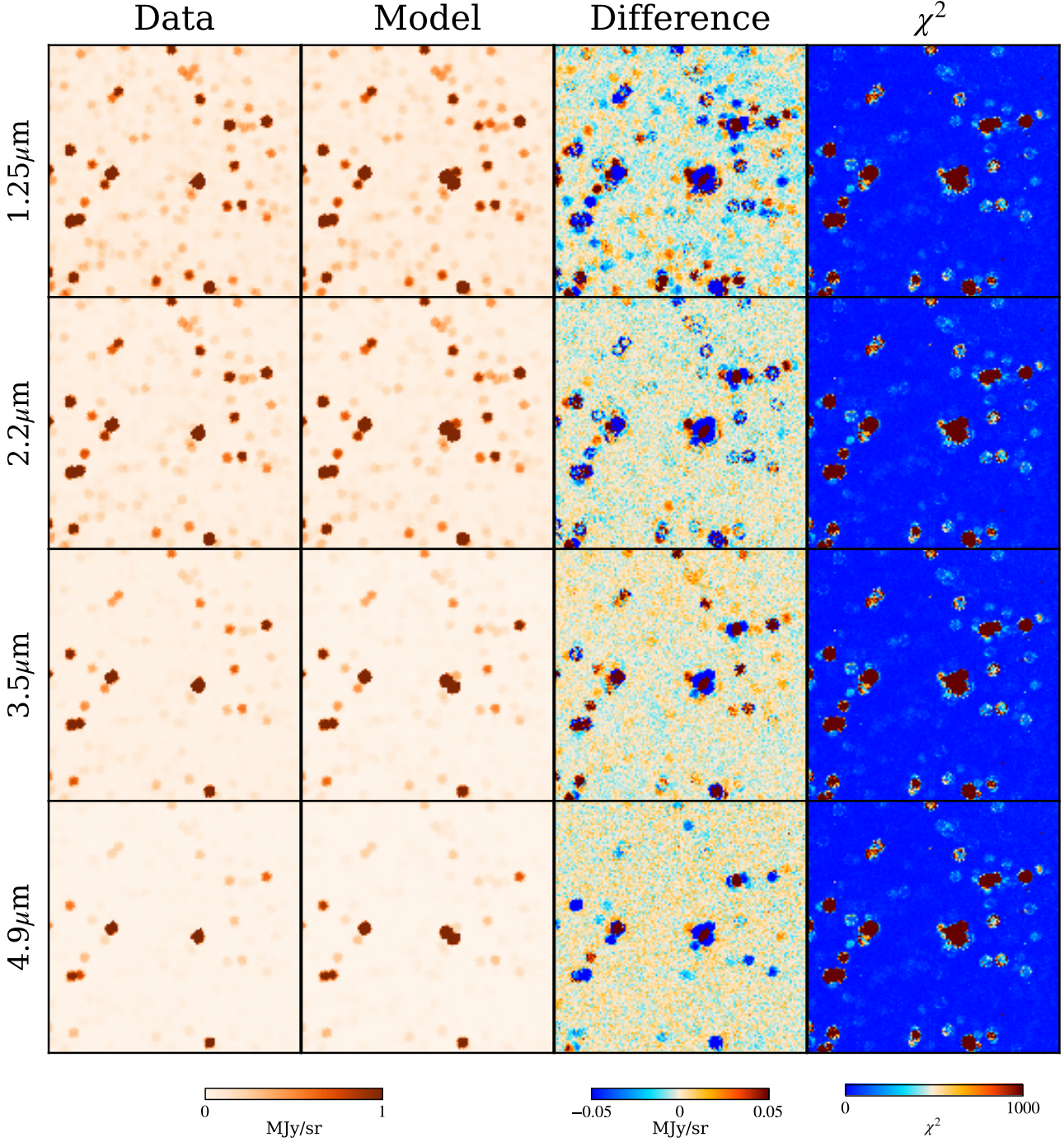
Fig. 9. Zoom-ins on a typical subregion of the sky centred at $(20^\circ, 70^\circ)$. The First and second columns show the map data and the total star model, respectively. The third column shows the (data-minus-model) difference between the two, and the final column shows the overall χ^2 of the component separation fit.

values of each parameter. We computed a total of 1090 unique samples spread over 5 independent chains after discarding our 25 samples of burn-in data.

In this paper, we present the results of the star models described in Sect. 2, and we direct interested readers to the companion papers for further information regarding the full framework. Specifically, details on the overall sampling approach can be found in Watts et al. (2024a); a new zodiacal light model is presented by San et al. (2024); a novel multi-component dust model is described by Gjerløw et al. (2026a), Sullivan et al. (2026) and Gjerløw et al. (2026b); and the final limits on the

CIB monopole derived from this work are presented by Watts et al. (2024b).

3.1. Maps

In Fig. 8 we show the mean star maps for the full pipeline run in all six DIRBE bands where they are modelled. Here, the maps show the sum of the bright stars component and the diffuse background, which accounts for the majority of the point source emission over the full sky. As expected, the emission is
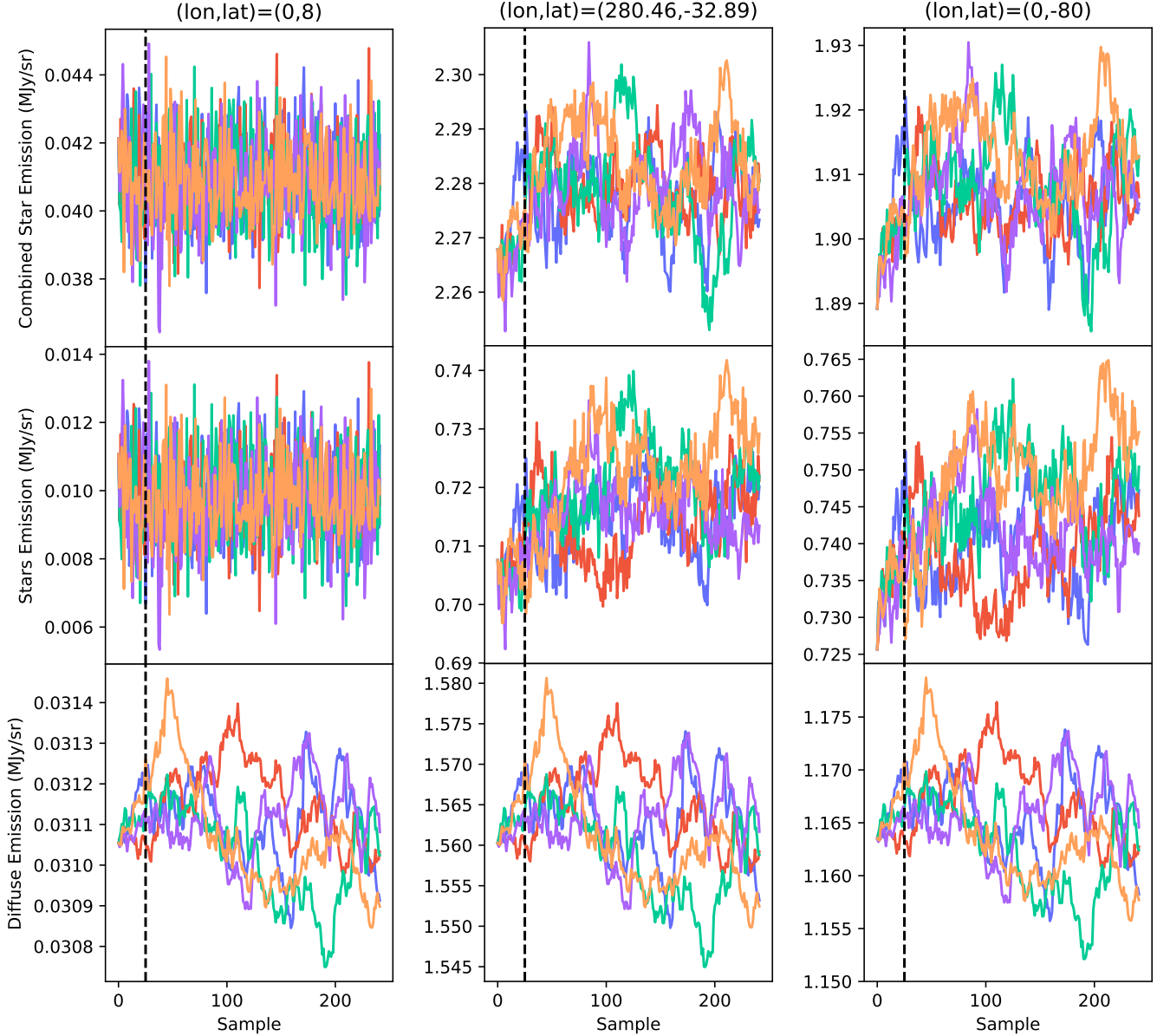
Fig. 10. Trace plots of the total star amplitude in all five chains for three pixels in different regions of the sky (low latitudes, the Large Magellanic Cloud and high latitudes) in the DIRBE 1.25 μm band. The dashed vertical lines indicate the end of the burn in period, and samples after that are included in our final sample set. The top row is the total star signal, and the bottom two rows are the bright stars and the diffuse template, respectively.

concentrated in the Galactic plane, but there is also an important contribution from high latitude stars.

In Fig. 9 we show zoom-ins of a typical 20° patch of sky centered at Galactic coordinates, $(l, b) = (20°, 70°)$, plotting the DIRBE sky map in each band for the four highest frequency bands where the stars are most significant. In the second column, we show the total star model for the same region, then the resulting residual, and finally the overall χ^2 of the fit. The residuals contain a variety of mis-modeled point sources.

We can identify three types of point source residuals in this third column of Fig. 9, although there are a large number of sources with residuals that are subdominant to the background noise level and so can be considered to be well modelled. Some of the point sources clearly show the imprints of spectral complexity, where the residual signature is blue in some bands and red in others, which implies that our knowledge of the spectra

is imperfect and a single overall amplitude fit will always be insufficient to model that source. The second class of residuals appear to be ring shapes, where the center of the point source is well modelled, but we oversubtract emission around the edges. This could be caused by our simplistic modelling of the DIRBE beams, which relies on the scanning strategy to symmetrize the otherwise square beam profile of the DIRBE instrument. The third type of residuals is more complex, and look to be superpositions of multiple sources in the same region. These residuals could possibly be reduced by pruning point sources from the model that are too close to one another, or potentially by improving our models of the brightest sources. No attempt to do so was made in this work, as these residuals were only a small fraction of the total sky, and can be handled by masking using the χ^2 values as a function of pixel, which clearly shows these same regions to be poorly modelled.
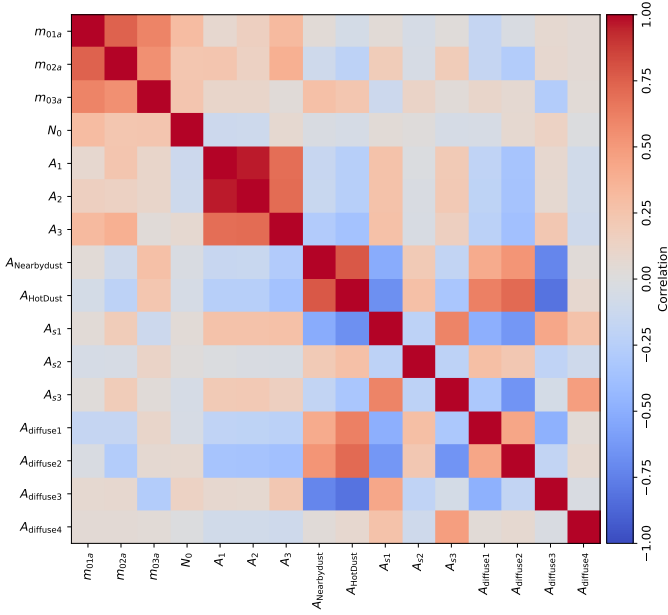
Fig. 11. Correlation among a selection of parameters relevant for star modelling. From top to bottom, the included parameters are 1-3) the monopoles for DIRBE channels between 1.25 and 4.9 μm; 4-7) zodiacal light cloud density, N_0, and albedoes, A_i, for the 1.25-3.5 μm bands; 8-9) full-sky dust amplitudes for the nearby and hot dust components; 10-12) the amplitudes of three randomly selected stars; and 13-16) the diffuse template amplitude for the 1.25-4.9 μm bands.

In Fig. 10, we show the total amplitude of the stars in three pixels in different regions in the sky (low Galactic latitudes, the Large Magellanic Cloud, and high Galactic latitudes) as a function of iteration, for all five of our independent sampling chains. The first 25 samples in each chain are discarded as burn in, and the remaining samples form the samples included in our analysis. We observe excellent Monte Carlo mixing in the top row, while the sky diffuse template amplitude mixes more slowly than the individual bright stars.

Figure 11 shows the correlation matrix computed over all 1090 accepted samples for a selected set of parameters, including monopoles for the 1.25-3.5 μm bands (the 4.9 μm monopole was not sampled, for details see Watts et al. (2024b)); four zodiacal light parameters (the cloud density, N_0, and the albedos for the 1.25-3.5 μm bands); two dust component amplitudes ($A_{\mathrm{NearbyDust}}$ and A_{HotDust}); the amplitudes of three randomly selected stars (A_{si}); and the diffuse starlight amplitude for the 1.25-4.9 μm bands. The strongest positive correlations are seen internally among the monopoles and among the zodiacal light parameters; these are further discussed by (Watts et al. 2024a; San et al. 2024). However, only a low level of correlations are observed between between these and the star model parameters. We do not see much cross correlation between the star parameters and other parameters in the global chain, with the exception of some of the individual star parameters and the dust amplitudes, which seem to vary. This suggests overall that the star parameters are only mildly degenerate with other full sky parameters.

3.2. Spectral Energy Densities

In addition to the amplitude maps at each frequency, we can also examine the SEDs of the sources within our model. Figure 12 shows the median SED model for all 424 829 bright star sources in our catalogue, as well as the SED for the diffuse template com-
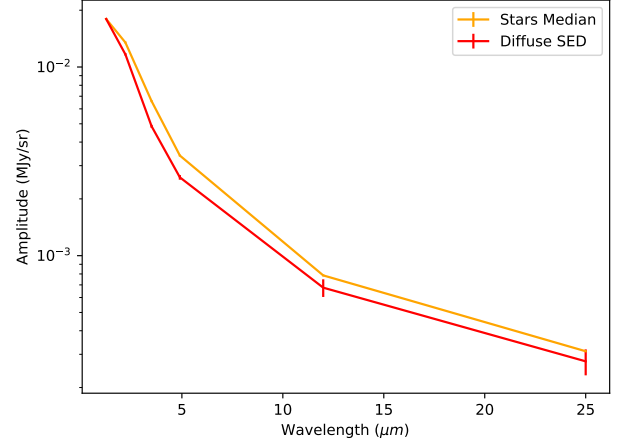
Fig. 12. Star emission as a function of wavelength. The orange line shows the median individual star, averaged over the five chains. The variance on this median are too small to be seen on the plot. The red curve shows the mean of the diffuse template SED fit to the data, with the error bars showing the variance across the Markov chains.
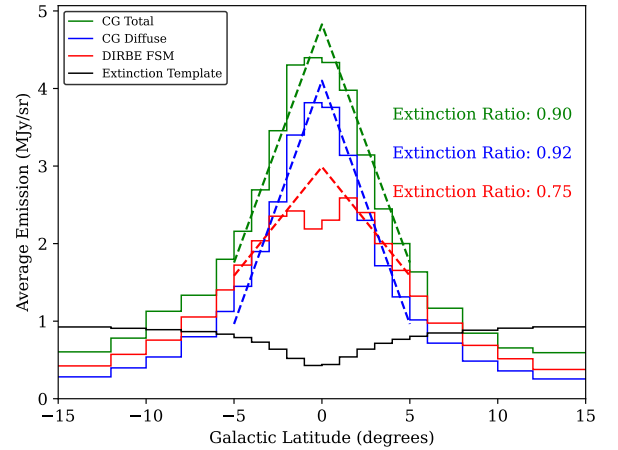
Fig. 13. Profiles of the DIRBE Faint Star Model (FSM) and CosmoGlobe star model as a function of galactic latitude. A linear extrapolation is overplotted in the core region from -5 to 5 degrees galactic latitude, but excluding the galactic center from -1 to 1 degree. The theoretical central value from this fit is compared to the measured values in the central bins to give estimates of the dust extinction in the galactic center for both cases.

ponent, both normalized to a common amplitude in the 1.25 μm band. These follow a similar overall shape, although the diffuse stars fall off faster than the bright stars with increasing wavelengths.

3.3. Extinction

We also investigate our model of extinction, to determine how it compares to other estimates. Figure 13 shows the mean star emission as a function of Galactic latitude, zoomed in on the central region. The three curves shows the DIRBE Faint Source Model used in the legacy analysis (Arendt et al. 1998), as well as our diffuse star model and the CosmoGlobe total star emission estimate. Overplotted as dashed lines are linear fits to the data

between 5 and 1 degrees, which, when extrapolated to the galactic center region, provides an approximation of the star signal in the absence of extinction. By comparing the peak amplitude of the fit to that of the models, we can approximate the magnitude of the extinction in the Galactic center, and this can be compared to the estimate from our extinction template (black line) which predicts about a 50% extinction. We see that the FSM estimates a ratio of around 0.75 in the central region of the galaxy, while our model predicts about 0.9, which is likely an underestimate of the total extinction on the sky. In particular, because our extinction correction is only applied to the bright sources, the diffuse template contribution (which accounts for three quarters of the total power) at $1.25\,\mu m$ is too bright in the Galactic center, leading to an overall underestimate of the extinction. Future work will aim to improve on this limitation of our model by taking into account the full 3D position of each star.

4. Comparison to other Analyses

4.1. DIRBE FSM

The original DIRBE analysis team (Arendt et al. 1998) also removed point sources from their measurement of the CIB emission, but followed a different approach. Instead of modelling the bright sources, the original analysis simply masked pixels brighter than a threshold (15 Jy at $1.25\,\mu m$), which resulted in cutting almost 35 % of the sky at $1.25\,\mu m$. For the diffuse sources, they build a model (the "faint source model" or FSM) using the methodology of Wainscoat et al. (1992), which integrates a model of source counts over the full sky, including models of Galactic morphology, 87 discrete source types, and the contribution from dust extinction. The top two panels of Fig. 14 compare our diffuse template with the FSM at $1.25\,\mu m$, where the latter has been converted from a QuadCube pixelization to HEALPix, and plotted at $N_{\mathrm{side}} = 256$.
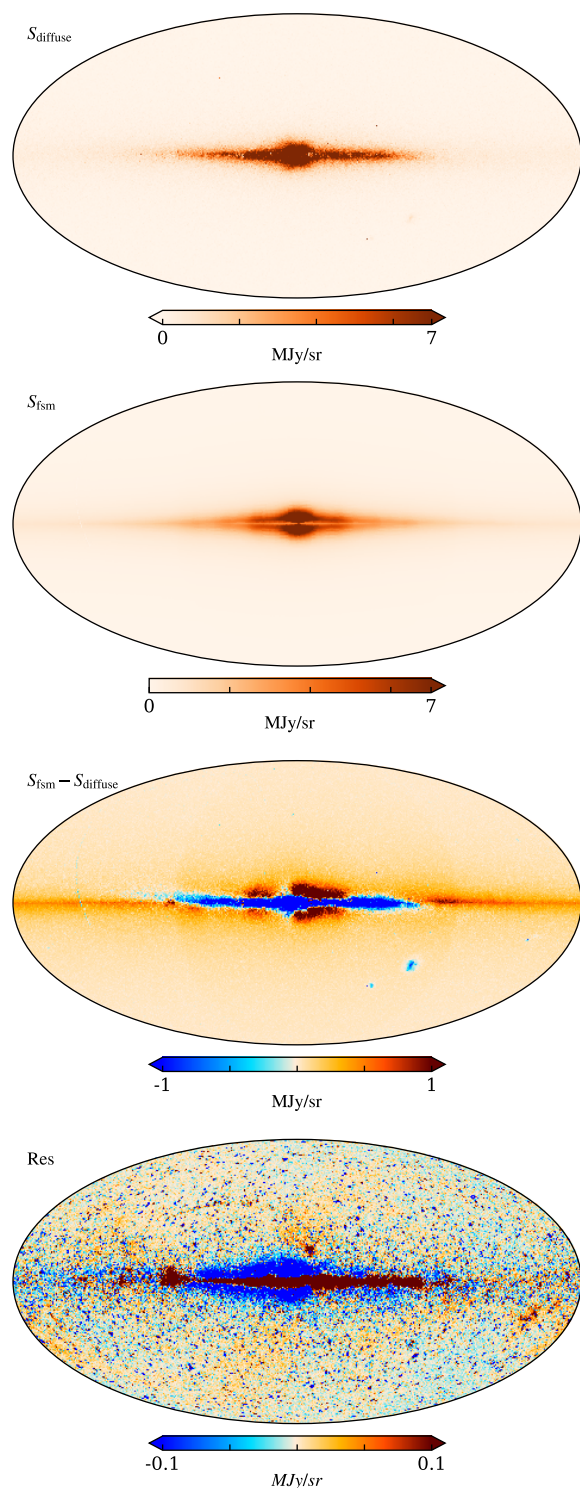
The third panel shows the difference between the two templates. This map shows that our model, based on the integrated AllWISE point source catalogue, predicts more star emission than the DIRBE FSM in the Galactic plane where dust extinction is dominant. However, when we look at the $1.25\,\mu m$ residual map in the bottom panel, it is clear that the model is actually underpredicting the signal in this region, and more extinction is therefore disfavoured by the data.

In the Galactic bulge, our model predicts less emission than the FSM, which, when we look at the bottom panel of Fig. 14, seems to be a better fit to the data. The blue residuals in the Galactic bulge show that the model overpredicts emission in general, and increasing the emission to the FSM level would result in a worse fit in this region.

4.2. DIRBE and 2MASS

After the official DIRBE analysis, Wright (2001) (following Gorjian et al. 2000) used the 2MASS catalogue to remove star emissions from DIRBE, aiming to derive an improved upper limit on the CIB monopole. Unfortunately, a positive detection was ultimately out of reach due to zodiacal light contamination. However, their analysis looked at four dark patches of the sky and used 2MASS to estimate the contribution of both bright (defined by a K-band magnitude lower than 14) and faint sources to the total signal in each patch. We compare these with the corresponding CosmoGlobe estimates in Table 2.

Differences in star classification between our analysis and Wright (2001) make it challenging to directly compare our amplitude estimates, but the sum of the bright and diffuse sources can still be compared. The CosmoGlobe analysis predicts about 40% more total star emission, depending on the field and the frequency, which is possibly due to having a deeper and more complete star catalogue than 2MASS. By successfully modelling and

Fig. 14. (Top panel:) CosmoGlobe diffuse star template. (Second panel:) DIRBE FSM at $1.25\,\mu m$ retrieved from LAMBDA and converted from QuadCube to HEALPix. (Third panel:) Difference between FSM and our diffuse template. (Bottom panel:) CosmoGlobe DR2 DIRBE $1.25\,\mu m$ residual map.

Patch	l (°)	b (°)	r (°)	Bright Stars (kJy/sr)		Diffuse Stars (kJy/sr)		Sum (kJy/sr)	
				Wright (2001)	Current	Wright (2001)	Current	Wright (2001)	Current
					1.25μm				
1	127.3	63.8	1.5	31.56	13.0	3.08	38.3	34.64	51.4
2	107.7	57.7	2.0	42.72	18.8	3.62	44.5	45.34	63.3
3	157.0	-82.7	2.0	40.89	20.0	2.94	40.0	43.83	60.1
4	257.8	-59.4	1.9	51.88	28.6	3.92	45.3	55.8	73.9
					2.2μm				
1	127.3	63.8	1.5	20.79	9.0	1.58	25.7	22.37	34.7
2	107.7	57.7	2.0	28.99	13.6	1.87	29.9	30.86	43.4
3	157.0	-82.7	2.0	28.62	15.1	1.50	26.9	30.12	42.0
4	257.8	-59.4	1.9	36.16	21.6	2.03	30.4	38.19	52.0

Table 2. Comparison of component intensities in selected fields from Wright (2001) and CosmoGlobe at 1.25 and 2.2 μm. Each field is defined by Galactic longitude and latitude center coordinates, (l, b), and a radius, r. The definitions of bright and diffuse sources differ between analyses, but the sum of the two allow reasonable comparison.
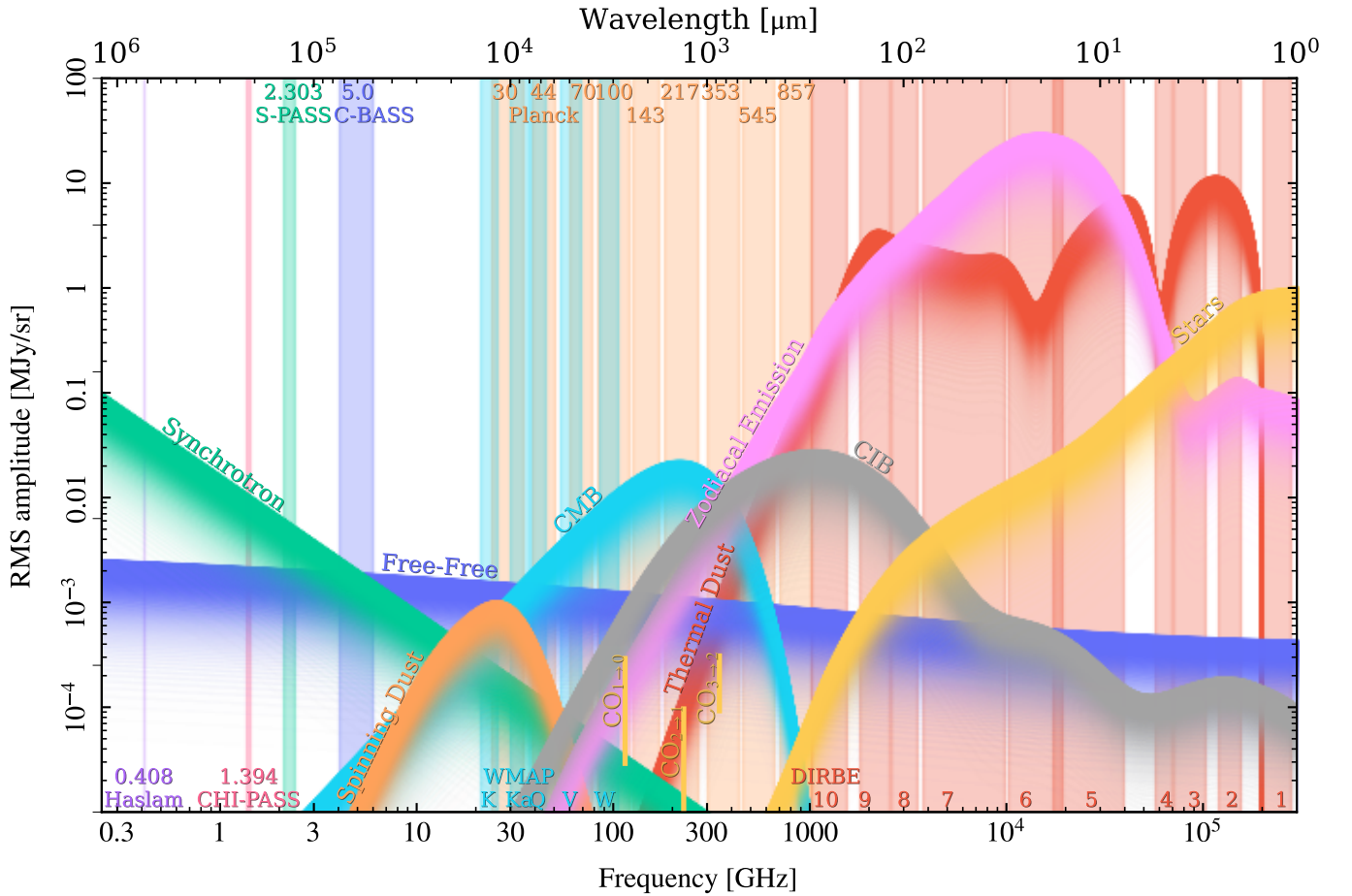
Fig. 15. Components of the infrared temperature sky from 1μm to 1m wavelengths. The approximate contribution from stars is shown in yellow, and the observing bands from various experiments are indicated by the vertical lines.

removing more star emission, we are able to improve upon their limits on the CIB, as discussed by Watts et al. (2024b).

5. Conclusions

Stars are a critical component of the infrared sky, which must be appropriately modelled in order to avoid contaminating other components. This paper has presented a model of the star emission for the DIRBE data that is able to account for the vast majority of the star signal in these measurements. Using data from *Gaia* and WISE we constructed models of 424 829 individual point sources as well as a diffuse background of the remaining 710 825 587 WISE sources, and together these account for 91% of the observed DIRBE flux density at 2.2μm, dropping to 1% at 25μm.

Figure 15 shows the full sky average star SED (yellow band) derived from this work, plotted together with the other main sky components as a function of frequency and wavelength, from radio to infrared frequencies. The CosmoGlobe DR2 sky model represents the first unified model of the microwave and infrared sky, and the star model presented here is an integral part of this work.

The star model showed robust Monte Carlo mixing properties within a Gibbs sampler, and it was able to fully describe the summed star emission in an effective manner. The resulting model was able to characterize and remove more star emission than earlier comparable works, in large part by using more modern data sets to trace star properties, and this consequently led to lower residuals and thereby stronger constraints on other astrophysical effects. Most notably, this work plays a critical role in a full-sky estimate of the CIB monopole that agrees with theoretical expectations around $1\mu m$, and properly including the deep background of diffuse stars turned out to be the critical component in this effort. Indeed, in a earlier iteration of this work we obtained an estimate of the CIB monopole at $1.25\,\mu m$ that was in line with previous results, and significantly higher than expected from theoretical modelling, and after a careful re-assessment of the end-to-end pipeline, we discovered a bug in the diffuse template implementation which had omitted the dimmest objects. Properly accounting for those sources was precisely what led to the final strong limits on the CIB monopole presented by Watts et al. (2024b).

While already the current work represents a significant step forward, there are still many improvements that can and will be implemented in the near future, and perhaps the single most important effect regards dust extinction. Although this paper incorporates a first-order extinction correction, this is based on a full-sky template taken from the *Planck E(B − V)* template that is derived by comparison with distant quasar data. To get accurate numbers for stars that are embedded in the Galaxy, we need to incorporate 3D position information from *Gaia* to determine the line-of-sight extinction for each source. Constructing a 3D model of all the stars and gas in our Galaxy is beyond the scope of this paper, but is a top-priority issue for future work.

A second improvement concerns the beam treatment. Instead of assuming the DIRBE beam to be azimuthally symmetric, it would be much better to account for the unique square shape of the DIRBE response function through a time-domain algorithm such as deconvolution mapmaking (Keihänen, E. & Reinecke, M. 2012), and perform beam deconvolution (or symmetrization) per sample. This could potentially resolve some of the "ring" residuals around bright sources reported in this paper.

Next, more accurate SEDs should be established for stars with $T_{\rm eff} > 12000K$. This may help reduce the residuals around the brightest sources, and this, combined with pruning nearby sources with vanishing amplitudes, could reduce the overall residual levels around the brightest sources. A more complete catalogue of star SEDs with higher resolution and expanded parameter ranges in the infrared would also improve the modelling of the individual sources, leading to lower residuals and fewer χ^2 cuts.

Finally, including additional high frequency data directly in the full run would be an important next step for this work, and will be the subject of future CosmoGlobe exploration. WISE is a prime candidate experiment for this work, but also AKARI (Murakami et al. 2007), *IRAS* (Neugebauer et al. 1984), and SPHEREx (Crill et al. 2020) will provide key information. Incorporating these data directly into the existing CosmoGlobe framework should provide enough extra information to constrain the star SEDs in the sampling stages instead of having to extrapolate them from other regimes.

References

Arendt, R. G., Odegard, N., Weiland, J. L., et al. 1998, ApJ, 508, 74
Arendt, R. G., Odegard, N., Weiland, J. L., et al. 1998, The Astrophysical Journal, 508, 74–105
BeyondPlanck Collaboration. 2023, A&A, 675, A1
Brown, A. G. A., Vallenari, A., Prusti, T., et al. 2018, Astronomy & Astrophysics, 616, A1
Crill, B. P., Werner, M., Akeson, R., et al. 2020, in Space Telescopes and Instrumentation 2020: Optical, Infrared, and Millimeter Wave, ed. M. Lystrup, N. Batalha, E. C. Tong, N. Siegler, & M. D. Perrin (SPIE)
Dickinson, C., Davies, R. D., & Davis, R. J. 2003, MNRAS, 341, 369
Fitzpatrick, E. L. & Massa, D. 1990, ApJS, 72, 163
Fitzpatrick, E. L., Massa, D., Gordon, K. D., Bohlin, R., & Clayton, G. C. 2019, ApJ, 886, 108
Gaia Collaboration, Brown, A. G. A., Vallenari, A., et al. 2018, A&A, 616, A1
Gaia Collaboration, Vallenari, A., Brown, A. G. A., et al. 2023, A&A, 674, A1
Galloway, M., Andersen, K. J., Aurlien, R., et al. 2023, A&A, 675, A3
Gardner, J. P., Mather, J. C., Clampin, M., et al. 2006, Space Science Reviews, 123, 485–606
Geman, S. & Geman, D. 1984, IEEE Trans. Pattern Anal. Mach. Intell., 6, 721
Gjerløw et al. 2026a, A&A, in preparation [arXiv:20xx.xxxxx]
Gjerløw et al. 2026b, A&A, in preparation [arXiv:20xx.xxxxx]
Gordon, K. D., Clayton, G. C., Decleir, M., et al. 2023, ApJ, 950, 86
Gorjian, V., Wright, E. L., & Chary, R. R. 2000, The Astrophysical Journal, 536, 550
Górski, K. M., Hivon, E., Banday, A. J., et al. 2005, ApJ, 622, 759
Hauser, M. G., Arendt, R. G., Kelsall, T., et al. 1998, ApJ, 508, 25
Husser, T.-O., Wende-von Berg, S., Dreizler, S., et al. 2013, Astronomy & Astrophysics, 553, A6
Keihänen, E. & Reinecke, M. 2012, A&A, 548, A110
Kelsall, T., Weiland, J. L., Franz, B. A., et al. 1998, ApJ, 508, 44

Kessler, M. F., Steinz, J. A., Anderegg, M. E., et al. 1996, A&A, 315, L27

Kuiper, G. P. 1938, ApJ, 88, 472

Murakami, H., Baba, H., Barthel, P., Clements, D. L., et al. 2007, Publications of the Astronomical Society of Japan, 59, S369

Neugebauer, G., Habing, H. J., van Duinen, R., et al. 1984, ApJ, 278, L1

Paradis, D., Dobashi, K., Shimoikura, T., et al. 2012, A&A, 543, A103

Planck Collaboration, Abergel, A., Ade, P. A. R., et al. 2014, A&A, 571, A11

Planck Collaboration X. 2016, A&A, 594, A10

San, M. et al. 2024, A&A, in preparation [arXiv:20xx.xxxxx]

Skrutskie, M. F., Cutri, R. M., Stiening, R., et al. 2006, AJ, 131, 1163

Sullivan et al. 2026, A&A, in preparation [arXiv:20xx.xxxxx]

Wainscoat, R. J., Cohen, M., Volk, K., Walker, H. J., & Schwartz, D. E. 1992, ApJS, 83, 111

Watts, D., Galloway, M., Gjerlow, E., et al. 2024a, A&A, submitted [arXiv:2408.10952]

Watts, D. et al. 2024b, A&A, in preparation [arXiv:2406.01491]

Watts, D. J., Basyrov, A., Eskilt, J. R., et al. 2023, A&A, 679, A143

Werner, M. W., Roellig, T. L., Low, F. J., et al. 2004, ApJS, 154, 1

Wright, E. L. 2001, The Astrophysical Journal, 553, 538–544

Wright, E. L., Eisenhardt, P. R. M., Mainzer, A. K., et al. 2010, The Astronomical Journal, 140, 1868–1881

Wright, E. L., Eisenhardt, P. R. M., Mainzer, A. K., et al. 2009, AllWISE Source Catalog

Zonca, A., Singer, L., Lenz, D., et al. 2019, Journal of Open Source Software, 4, 1298